Ultralong Cycle Life for Deep Potassium Storage Enabled by BiOCl/MXene van der Waals Heterostructures

Xin Cao,[#a] *Yuying You*,[#a] *Dawei Sha*,[a] *Huan Xia*,[a] *Hang Wang*,[b] *Jing Zhang*,[b] *Rongxiang Hu*,[a] *Yicheng Wei*,[a] *Zhuoheng Bao*,[a] *Yang Xu*,[c] *Long Pan*,[a] *Chengjie Lu*,*[a] *Wei He*,*[a] *Min Zhou*,*[b] *and ZhengMing Sun**[a]

a. School of Materials Science and Engineering, Southeast University, Nanjing, Jiangsu 211189, P. R. China

b. Hefei National Laboratory for Physical Sciences at the Microscale, University of Science and Technology of China, Hefei, Anhui, 230026, P. R. China

c. Department of Chemistry, University College London, WC1H 0AJ, UK

*Email: zmsun@seu.edu.cn (Z.M.S.); mzchem@ustc.edu.cn (M.Z.);weih@seu.edu.cn (W.H.); lucj008@126.com (J.C.L.)

[#] These authors have equal contributions to this work.

Abstract

Conversion/alloying-type anodes are drawing attention due to their high theoretical capacities, but inferior reversibility, especially under low current densities, has hampered potential applications. Conventional strategies mainly focus on conversion/alloying processes, whereas the intercalation process is rarely analyzed. Herein, the intercalation process has been correlated with conversion/alloying processes by ion dispersion states. BiOCl/$Ti_3C_2T_x$ MXene van der Waals heterostructure has been selected as a proof-of-concept system. Multifunctional MXenes not only contribute to atomic dispersion and boosted ion diffusion at the 1st cycle by constructing a novel

heterostructure but serve as supporting frameworks to sustain long-term structural stability. Consequently, a cell with BiOCl/MXene anode delivers an ultralong cycle-life of running over ten months, maintaining a high capacity of 225 mAh g^{-1} over 1300 cycles at 100 mA g^{-1} and a retention of 81.3%. These findings verify that enhanced initial intercalation can facilitate higher reversibility and shed light on developing high-performance conversion/alloying-type anodes.

1. Introduction

Potassium-ion batteries have been regarded as a promising electrochemical storage system for grid-scale applications due to their low comprehensive cost, receiving ever-growing attention.[1-3] In terms of potassium-ion host material design, conversion/alloying-type anode materials represented by group 14 and 15 element-based metals and their compounds have been energetically developed because of their high potassium storage capacities. Nevertheless, the practical commercialization of conversion/alloying-type anodes for potassium-ion batteries has not been realized yet, due to their severe capacity fading and cycling instability.[4] The major solutions have been focused on nanoconfinement engineering and introducing conductive skeletons. [5-8] With these efforts, the reversibility has been improved and the performance deterioration has been retarded. Nonetheless, an important issue has been neglected when these reported optimized conversion/alloying-type anodes to work at a low current density, an exacerbated capacity decay has been frequently observed and the corresponding cycle life together with high capacities is very limited, induced by a more complete alloying/de-alloying process.[9, 10] Noteworthily, compared with cycling stability at higher current densities which mainly depends on capacitive reactions, cycling stability at lower current density imposes more strict demands on the intrinsic structure reliability of electrode materials and may encounter greater implementation difficulties. Moreover, cycling performance at a low current density also matters owing to their unique application scenarios. For example, power supply stability will become the top priority in potential working scenarios like marine navigation beacons and signal lights used in highways and railways. Considering the importance of anode properties at a low current density, it is necessary to explore the mechanism of fading and develop an efficient strategy to improve cycling stability.

Regarding the electrochemistry of most conversion/alloying-type anodes, potassiation

reactions usually start with an intercalation process, similar to lithiation and sodiation reactions. [3, 11, 12] In this way, a certain number of potassium ions will first intercalate into the anodes to generate potassium-containing phases during the initial discharge process. Subsequently, along with the intercalation of more potassium ions, conversion reactions occur and new potassium-rich phases formed. The potassiation reactions have shown a close relevance between the intercalation process and the conversion process. Previous reports have found that the presence of the intercalation stage during the potassiation process of conversion/alloying-type anodes tends to render a gradual volume variation and thereby improves the whole cyclic stability.[13-15] Under a reasonable design of the intercalation process, even some materials that are originally inert to conversion can go through conversion reactions.[14] These findings imply that improved intercalation may help stabilize the conversion/alloying stage and further confirm that the intercalation stage will exert effects on the subsequent conversion and alloying/de-alloying reactions. However, the detailed correlation that exists between the intercalation stage and conversion/alloying stages has not been clarified so far. Generally, the potassium ion diffusion tends to be more and more difficult when they intercalate from the surface to the inner lattice of electrodes, resulting in incomplete conversion and alloying/de-alloying reactions and the formation of uneven alloy phases. In order to better reflect the diffusion depth of ions and evaluate what effects the ion intercalated intermediate phases will have on the following conversion/alloying reactions, dispersion degrees of potassium ions have been adopted to describe the potassium ion concentration gradient after the intercalation stage. On this basis, anodes with different dispersity degrees of potassium ions during the intercalation process can serve as control samples to illustrate the correlations between the intercalation stage and the conversion stage. Initiated by potassium ion intercalation, the conversion process is expected to be improved by optimized intercalation which can render higher potassiation degrees of anodes. Herein, optimized intercalation is ensured by constructing a novel van der Waals heterostructure and the heterostructure may be advantageous to electrochemical kinetics and can facilitate atomic dispersion of potassium ions via enhanced intercalation. [16, 17]

In this work, the dispersity of potassium ions has been proposed to correlate the initial intercalation process with the following conversion and alloying/de-alloying processes. Bismuth oxychloride (BiOCl) has been chosen as a model material, sharing the common issue with other conversion/alloying-type anodes and possessing high theoretical specific capacities (618 mAh g^{-1}

or 4771 mAh cm^{-3}) and low redox potential.[5, 18, 19] As a proof-of-concept demonstration, two model systems with different dispersion states of potassium ions during the initial intercalation processes, the BiOCl nanosheets and BiOCl/$Ti_3C_2T_x$ MXene (transitional metal carbides, nitrides, and carbonitrides[20, 21]) with van der Waals heterostructure, are compared to reveal the influence of the intercalation of potassium ions on the cycling stability. Benefitting from the structure merits, the BiOCl/$Ti_3C_2T_x$ MXene heterostructure anode tends to have rich potassium ions dispersed during the early stage of discharging process. This good dispersity of potassium ions during the initial stage guarantees that the fabricated anode can achieve stable alloying/de-alloying reactions during the following cycling process, accompanied by higher coulombic efficiency and smaller capacity loss. More encouragingly, the BiOCl/$Ti_3C_2T_x$ MXene anode exhibits an ultralong stable cycling performance of remaining 225 mAh g^{-1} over 1300 cycles at a low current density of 0.1 A g^{-1}, with a high capacity retention of 81.3%. Notably, the whole running time is beyond 10 months and this implies a good commercial prospect for the BiOCl/$Ti_3C_2T_x$ MXene anode.

2. Results and discussion

2.1 Synthesis and Characterization of BiOCl/MXene van der Waals Heterostructure

Preparation of the BiOCl/$Ti_3C_2T_x$ MXene heterostructure was based on an electrostatic self-assembly strategy. As shown in **Figure S1a**, Supporting Information, BiOCl nanosheets were homogeneously distributed across the wrinkled surface of $Ti_3C_2T_x$ MXenes. The lamellar structure features were well inherited from the pristine BiOCl and MXene nanosheets (**Figure S1b and S1c**, Supporting Information), demonstrating a successful assembly. This can be further confirmed by the zeta potential investigation in Figure S2, Supporting Information. Furthermore, benefitting from the electrostatic interactions, the BiOCl nanosheets were fixed closely on the highly conductive MXene substrates. Meanwhile, the repulsion forces between similarly charged nanosheets can ensure the uniformity and stability of the whole structure.[22]

To further validate the successful assembly of the hybrid, a typical transmission electron microscopy (TEM) image of BiOCl/$Ti_3C_2T_x$ MXene can be seen in **Figure 1a**. Both BiOCl and $Ti_3C_2T_x$ MXene sustained 2D morphology, and BiOCl nanosheets with a diameter of about 150−300 nm were uniformly distributed on the $Ti_3C_2T_x$ MXene substrates. Compared with the initial morphologies of pure BiOCl and MXene nanosheets (**Figure S1d and S1e**, Supporting Information), the BiOCl/$Ti_3C_2T_x$ MXene commendably maintained the 2D characteristics without obvious

structure changes, further confirming the successful integration of the hybrid. The selective area electron diffraction (SAED) pattern (**Figure 1b**) denoted two sets of diffraction rings, derived from BiOCl and $Ti_3C_2T_x$ MXenes respectively. Depending on beam-focusing conditions, (110) and (100) planes of $Ti_3C_2T_x$ MXenes and (110) and (200) planes of BiOCl were both viewed along the [001] zone axis. These observed diffraction spots indicated that (001) planes were highly exposed in tetragonal BiOCl and hexagonal $Ti_3C_2T_x$ MXenes, which was consistent with their 2D layered structure features. Noteworthily, the face-to-face contact between BiOCl and $Ti_3C_2T_x$ MXene nanosheets guaranteed a good vertical combination, boosting the formation of a heterostructure interface. This can be further verified by the high-resolution TEM image in **Figure 1c**, which illustrated the detailed boundary between BiOCl and $Ti_3C_2T_x$ MXenes. The elemental distribution was determined by the elemental dispersive X-ray spectroscopy (EDS) mappings and high-angle annular dark-field scanning transmission electron microscopy (HAADF-STEM) image in **Figure 1d**. The Bi, Cl, O, Ti, and C elements were all well distributed throughout the whole BiOCl/$Ti_3C_2T_x$ MXene hybrid, which was in agreement with the SEM and TEM results.

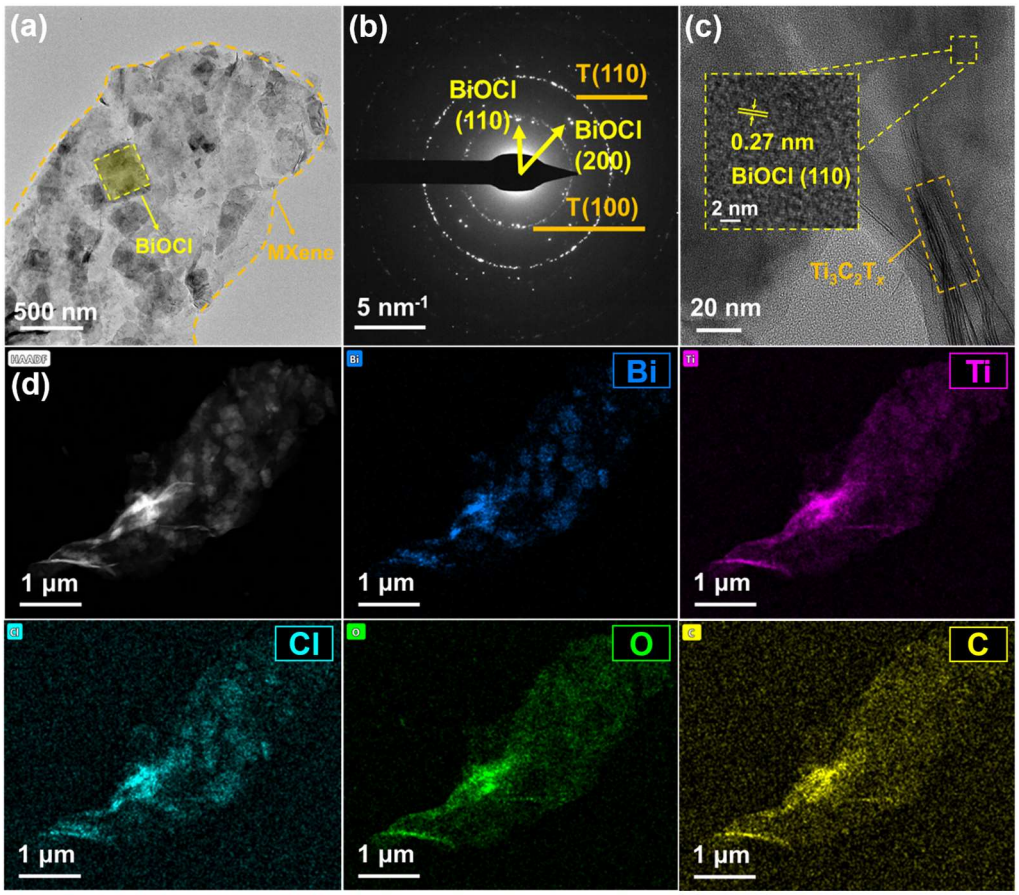

Figure 1 Morphology characterizations: a) TEM image of BiOCl/$Ti_3C_2T_x$ MXene; b) SAED pattern of BiOCl/$Ti_3C_2T_x$ MXene; c) HRTEM image of the interface between BiOCl and $Ti_3C_2T_x$ MXene; d) HAADF-STEM image and EDS mappings of Bi, Cl, O, Ti, and C of BiOCl/$Ti_3C_2T_x$ MXene.

In order to identify the phase structure of BiOCl/$Ti_3C_2T_x$ MXene, the precursors including BiOCl and $Ti_3C_2T_x$ MXenes were selected as the contrast samples. To start with, the phase composition and crystal structure of BiOCl, $Ti_3C_2T_x$ MXenes, and BiOCl/$Ti_3C_2T_x$ MXene were revealed by X-ray diffraction (XRD) patterns in **Figure 2a**. The diffraction peaks of pure BiOCl were nearly identical to the standard tetragonal BiOCl (PDF#06-0249). The main peak located at 6.7° in the XRD pattern of $Ti_3C_2T_x$ MXenes was indexed to the (002) crystal plane. When BiOCl/$Ti_3C_2T_x$ MXene was synthesized, all of the characteristic peaks from BiOCl and $Ti_3C_2T_x$ MXenes were reserved and no new peaks were noticed. This implied that BiOCl and $Ti_3C_2T_x$ MXenes still maintained their independent phases in the hybrid, indicating good compatibility between these two original precursors. Note that the (002) facet shifted to the lower angle (from 6.7° to 5.9°) compared with pure $Ti_3C_2T_x$ MXenes, resulting from expanded interlayer spacing. To further investigate the interactions between BiOCl and $Ti_3C_2T_x$ MXenes, Raman spectroscopy was

performed. In **Figure 2b**, the Raman bands at 1334.6 cm^{-1} and 1574.6 cm^{-1} corresponding to D and G peaks were retained in BiOCl/$Ti_3C_2T_x$ MXene, indicating the maintenance of layered structure of MXene.[23] Additionally, the vibrational peaks situated at 257.8 cm^{-1}, 419.5 cm^{-1}, and 606.4 cm^{-1} (marked as peak I, II, and III) were also assigned to $Ti_3C_2T_x$ MXenes. Compared with the pure $Ti_3C_2T_x$ MXenes, peak I and II, associated with A_{1g} and E_g vibration mode of terminal group region,[24-26] were found red-shifted and blue-shifted respectively, suggesting the fabrication of hybrid may principally depend on the interlamellar interaction.[27] Meanwhile, Raman fingerprints of BiOCl were detected at 128.4 cm^{-1}, 150.1 cm^{-1}, and 190.7 cm^{-1} in the spectra of hybrid, ascribed to the out-of-plane A_{1g} peaks and in-plane E_g peaks of the Bi-Cl stretching mode.[28, 29] A similar peak shift tendency was noticed here and once again proved that the hybrid was built based on interlayer forces. The detailed surface chemical states and chemical bonding of BiOCl/$Ti_3C_2T_x$ MXene were clarified by X-ray photoelectron (XPS) measurements. According to the full XPS survey spectrum of BiOCl/$Ti_3C_2T_x$ MXene depicted in **Figure S3**, Supporting Information, the presence of Bi, O, Cl, Ti, and C elements was confirmed, verifying the successful integration of BiOCl and $Ti_3C_2T_x$ MXenes. As plotted in **Figure 2c**, the high-resolution Bi 4f spectra of BiOCl/$Ti_3C_2T_x$ MXene were analogous to that of pristine BiOCl, and two peaks at 164.5 eV and 159.2 eV were attributed to Bi $4f_{5/2}$ and Bi $4f_{7/2}$ orbitals.[30] In **Figure 2d**, the magnified Ti 2p spectra of BiOCl/$Ti_3C_2T_x$ MXene and $Ti_3C_2T_x$ MXenes were also compared and both of them contained three pairs of peaks representing Ti−C, Ti (II), and Ti−O.[31-33] It should be pointed out that the deconvoluted subpeaks in Ti 2p spectra experienced a slight decrease trend towards low binding energy region but those in Bi 4f spectra shifted contrariwise. The electron cloud motion preference for BiOCl layers was correlated with the formation of the heterostructure, where highly conductive MXenes can give a current injection into BiOCl by virtue of a built-in electric field. The high-resolution O 1s, Cl 2p, and C 1s spectra of BiOCl/$Ti_3C_2T_x$ MXene were also recorded and there was no new bond in comparison with pristine BiOCl and $Ti_3C_2T_x$ MXenes (**Figure S4 and S5**, Supporting Information). These results confirmed that BiOCl/$Ti_3C_2T_x$ MXene only contained two independent phases, BiOCl and MXenes, and no new phases were generated. Based on the XPS analysis, the conclusion can be established that the interaction between BiOCl and $Ti_3C_2T_x$ MXenes in the heterostructure is van der Waals force and the synthesized BiOCl/$Ti_3C_2T_x$ MXene is a van der Waals heterostructure.[16] It should be stressed here that there still exists van der Waals interactions

between BiOCl and $Ti_3C_2T_x$ MXenes, making the heterostructure distinctively different from composites. The interface-tailored heterostructure is supposed to improve potassium ion intercalation and may well exert positive effects on potassium ion storage.

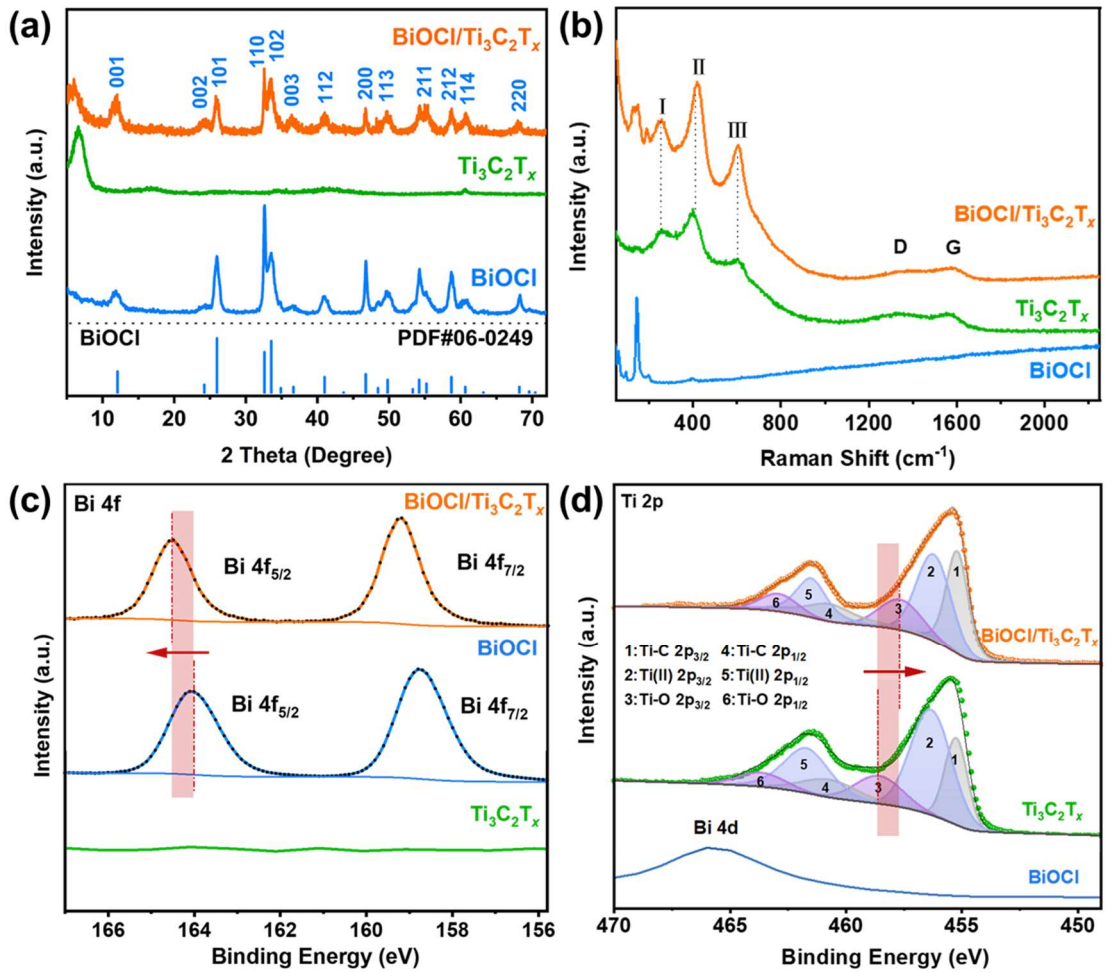

Figure 2 Componential and structural characterizations: a) XRD patterns of $BiOCl/Ti_3C_2T_x$ MXene, $Ti_3C_2T_x$ MXenes, and BiOCl; b) Raman spectra of $BiOCl/Ti_3C_2T_x$ MXene, $Ti_3C_2T_x$ MXenes, and BiOCl; c) High-resolution XPS spectra of Bi 4f in $BiOCl/Ti_3C_2T_x$ MXene, BiOCl, and $Ti_3C_2T_x$ MXenes; d) High-resolution XPS spectra of Ti 2p in $BiOCl/Ti_3C_2T_x$ MXene, BiOCl, and $Ti_3C_2T_x$ MXenes.

2.2 Electrochemical Properties of Potassium-Ion Batteries

Introducing vertical heterojunction between the dissimilar materials allows easier ion intercalation and diffusion through the atomically sharp heterointerface and thus the designed $BiOCl/Ti_3C_2T_x$ MXene van der Waals heterostructure was assessed as the anode for potassium-ion batteries. The effects of composition ratios were considered and the composition ratio has been optimized in advance (**Figure S6**, Supporting Information).

As given by **Figure 3a**, the initial three cycles of cyclic voltammetry (CV) curves at a sweep rate of 0.1 mV s^{-1} showed the electrochemical behavior of the heterostructure electrode. During the initial discharge process, a broad peak near 1.71 V correlated with the intercalation of potassium ions first appeared, followed by a strong peak around 1.50 V which was indicative of the irreversible conversion reaction from BiOCl to metallic Bi.[5] The residual cathodic peaks denoted the multistep alloying process for bismuth, accompanied by the growth of a solid electrolyte interface. In the subsequent cycles, all the curves featured anodic peaks around 0.60 V and 1.27 V standing for the depotassiation process and cathodic peaks around 0.10 V and 0.73 V standing for potassiation process, indicating high stability of alloying/de-alloying reactions.[34-37] The potassium ion storage process can be mainly divided into three stages: intercalation stage, conversion stage, and alloying/de-alloying stage. Moreover, the possible reaction process was proposed as the following equations: [38, 39]

Intercalation stage: $BiOCl + xK^+ + xe^- \rightarrow K_xBiOCl;$

Conversion stage: $K_xBiOCl + (3\text{-}x)\ K^+ + (3\text{-}x)\ e^- \rightarrow Bi + K_2O + KCl\ (dissolved);$

Alloying/de-alloying stage:

$$Bi + K^+ + e^- \rightarrow KBi\ ;$$

$$KBi + 2K^+ + 2e^- \rightarrow K_3Bi\ ;$$

$$K_3Bi - 2K^+ - 2e^- \rightarrow KBi;$$

$$KBi - K^+ - e^- \rightarrow Bi$$

The potassium ion storage behavior was further validated by the galvanostatic charge−discharge (GCD) curves gained at a current density of 100 mA g^{-1} in **Figure 3b**. The plateaus here well matched with the redox peaks in CV profiles. It should be emphasized that a discernible discharge plateau at 1.70 V was observed during the early time of the first discharge step. This could be attributed to the potassium ion intercalation reaction and more attention should be given to clarifying the role of the intercalation stage. Additionally, the BiOCl/MXene anode shared a similar electrochemical behavior with BiOCl, and BiOCl was considered as the main capacity contributor for potassium ion storage. Meanwhile, as shown in Figure S7, Supporting Information, the potassium storage capability of MXene was inferior to BiOCl and pristine MXene anode can only deliver a capacity of less than 50 mAh g^{-1} after ten cycles at 100 mA g^{-1}. In this regard, MXene itself can make a pretty limited contribution to the potassium storage capacity, further confirming

the reliability to analyze the electrochemistry mainly based on BiOCl.

As seen in **Figure S8**, Supporting Information, the BiOCl/MXene anode still can reversibly carry out potassium ion storage even after 50 consecutive cycles at 0.3 mV s^{-1}, resulting from impressive cycling durability. More encouragingly, when evaluating the long-term stability (**Figure 3c**), the BiOCl/MXene anode delivered a specific capacity of 225 mAh g^{-1} after 1335 cycles at a low current density of 100 mA g^{-1}, with a retention ratio of 81.3% (this value is calculated relative to 276.7 mAh g^{-1} at tenth cycle). A short-period capacity loss appeared during the very early cycling process and this mainly resulted from the irreversibility of conversion reactions. The whole running time was beyond 10 months and the ultimate coulombic efficiency remained at 99.9% which was very close to 100%. To the best of our knowledge, a calendar life of 10 months is the longest among the reported conversion/alloying-type anodes for potassium-ion batteries, exhibiting ultra-stable cycling performance. Encouragingly, this cycle life is also comparable to quite a few intercalation-type anodes, as shown in **Figure S9**, Supporting Information. The unprecedented cycle life made the BiOCl/MXene anode greatly promising for commercial use and was beneficial to pushing forward the commercialization of the conversion/alloying-type anode materials. This exciting performance may principally benefit from the introduced heterointerface. It may greatly facilitate initial potassium ion intercalation and thus achieve atomically homogeneous dispersion of potassium ions. Such a good dispersion state boosted by optimized intercalation ensured thorough preliminary conversion and alloying reactions, confirmed by a relatively high initial coulombic efficiency of 69.23%, and was highly conducive to the steady operation of subsequent alloying/de-alloying reactions. In contrast, the pristine BiOCl anode underwent a dramatic capacity fall during the initial 100 cycles (the coulombic efficiency of BiOCl anode in Figure 3c has been replotted in Figure S10, Supporting Information). A worse dispersion state of potassium ions before the conversion stage and the lack of diffusion pathways may be the reasons behind.

To further validate our hypothesis focusing on the potassium ion dispersion, a comparison between the BiOCl/MXene heterostructure and the mechanical mixtures of BiOCl and MXene with the same weight ratio was made to exclude the influences of conductivity. As shown in **Figure S11a and S11b**, Supporting Information, their chemical composition was almost the same. According to the SEM image in **Figure S11c**, Supporting Information, the mechanically mixed BiOCl and MXenes presented uneven distribution and a tendency of agglomeration. Correspondingly, as seen

in **Figure S11d and S11e**, Supporting Information, the mechanical mixtures displayed inferior electrochemical performance, and the specific capacity decreased rapidly during the early cycling stage. Therefore, it is reasonable to exclude the impacts of conductivity.

As stated earlier, the stable cycling performance was deduced to be closely linked with the thorough initial discharge process. To build up a better picture of the early stage of alloying/de-alloying course, the coulombic efficiency comparison was made. In **Figure 3d**, the coulombic efficiency of the BiOCl/MXene anode was appreciably higher than the BiOCl anode and fast recovered to ~98% at the eighth cycle. The higher reversibility indicated more complete conversion and alloying/de-alloying reactions in BiOCl/MXene anode. This could be attributed to the improved dispersion states of potassium ions during the initial intercalation process by virtue of the van der Waals heterostructure. For comparison, without the assistance of the heterointerface, the bulk BiOCl nanosheets tend to exhibit lower reversibility, possibly due to a bad potassium ion dispersion state and the difficult ion diffusion. Besides, both BiOCl and BiOCl/MXene anodes showed lower coulombic efficiencies in the first cycle than those in the subsequent cycles. This should be correlated with the irreversibility of conversion reactions.

In **Figure 3e**, the cycling performance comparison covering capacity retention, cycle number, and specific capacity, was made between the previously reported Bi-based anodes for potassium-ion batteries and our work.[5, 6, 9, 10, 38-52] The BiOCl/MXene anode in our work remarkably outperformed its counterparts. The detailed data has been summarized in **Table S1**, Supporting Information.

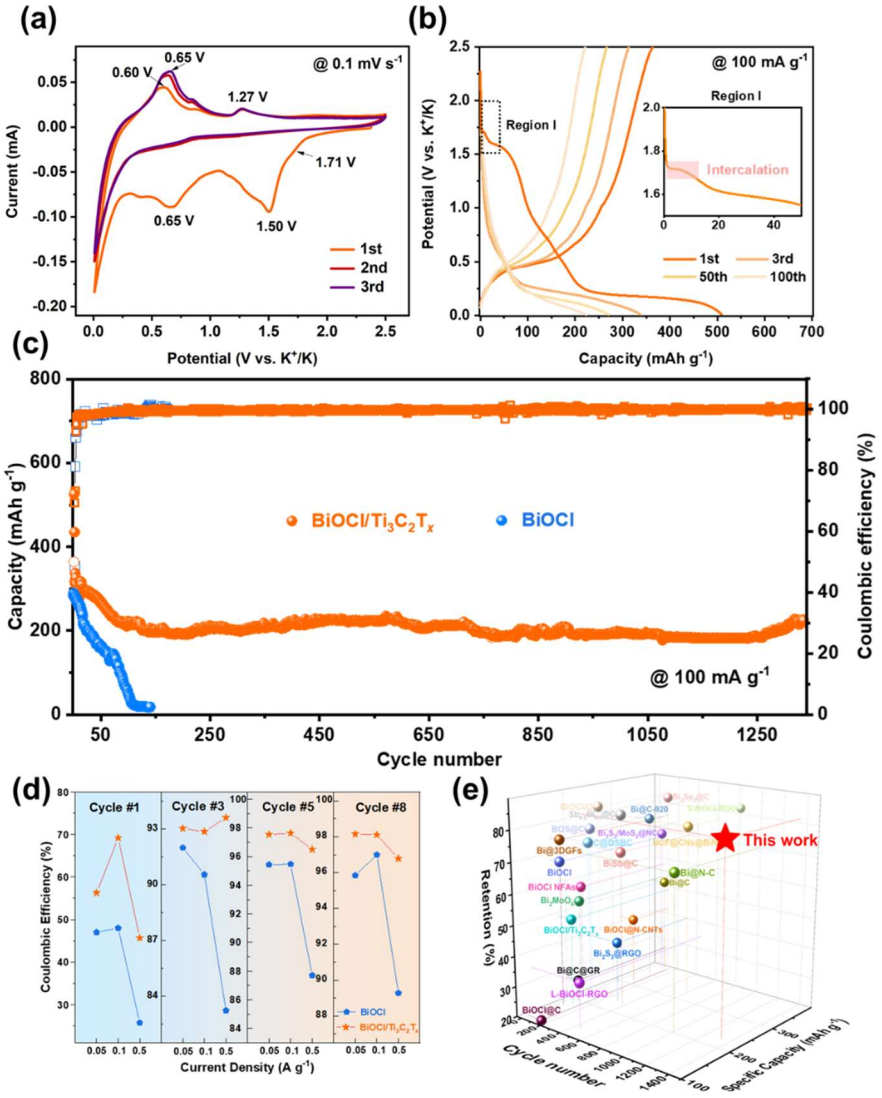

Figure 3 Electrochemical performance: a) CV curves of BiOCl/MXene anode at a scan rate of 0.1 mV s^{-1}; b) GCD curves of BiOCl/MXene anode at 100 mA g^{-1}; c) Cycling performance of BiOCl/ MXene and BiOCl anodes at 100 mA g^{-1}; d) The comparison of coulombic efficiencies of BiOCl/ MXene and BiOCl anodes during the initial cycling process; (e) Cycling performance of BiOCl/MXene anode and other previously reported bismuth-based anodes for potassium-ion batteries.

2.3 Insights into Superior Long-Term Cycling Stability

When it comes to the origin of the stable ultralong cycling performance of BiOCl/MXene anode, the electrochemical reaction kinetics were first analyzed. Electrochemical impedance spectroscopy (EIS) has been investigated toward electrodes at electrochemically stable states to better understand the ion diffusion and electron transfer behaviors. The Nyquist plots acquired at full-discharge and full-charge states in the first cycling course have been shown in **Figure 4a** and **Figure 4b**. The semicircles at the high-frequency region are related to the charge transfer resistance (R_{ct}), which is assumed as a critical indicator of electrochemical kinetics. R_{ct} varied with the states

of charge and the specific values of R_{ct} were summarized in **Figure 4c**. At the full discharged state, R_{ct} occupied the largest proportion of the total resistance of the battery system. The BiOCl/MXene anode exhibited much smaller R_{ct} (1101 Ω) than the BiOCl anode (2798 Ω). This indicated that the BiOCl anode had lower reaction reversibility and experienced more incomplete conversion and alloying reactions, suffering from a blocked intercalation process and poor atomically dispersed potassium ions. But for the BiOCl/MXene anode, benefitting from the built-in electric field introduced by unique heterostructure, facile ion diffusion and electron transfer have been achieved, ameliorating the dispersion state of potassium ions and reaction reversibility. When completely charged, R_{ct} value of BiOCl anode was 86 percent larger than its counterpart and displayed inferior charge transfer capability. Notably, as shown in **Figure S12** Supporting Information, R_{ct} of the heterostructure anode remained unvaried while that of BiOCl anode apparently increased. This convincingly demonstrated that a good dispersion state acquired during the initial intercalation stage can bring about excellent kinetics and strongly guarantee stable subsequent alloying/de-alloying reactions.

The diffusion of potassium ions was also evaluated based on the Warburg element in the low-frequency region of EIS. The diffusion coefficients were calculated based on the following equation: $D= (R^2T^2)/(2A^2n^4F^4C^4\sigma^2)$, and R, T, A, n, F, C, and σ stood for the gas constant, absolute temperature, surface area of the electrode, transferred electron number per molecular, Faraday constant, the ion molar concentration in the bulk electrode, and Warburg factor, respectively. Among them, Warburg factor σ was obtained through the relationship between the real part of impedance Z' and angular frequency ω ($Z'=R_{ct}+R_s+\sigma\omega^{-1/2}$, where R_s represented the ohmic resistance). As fitted in **Figure S13** Supporting Information, the values of Warburg contribution and diffusion coefficients were figured out. The higher diffusion coefficients of heterostructure anode than BiOCl anode implied better potassium ion diffusion kinetics, further justifying the superiority of the heterostructure for achieving a good dispersion state of potassium ions. In addition, galvanostatic intermittent titration technique (GITT) was employed to further assess the potassium ion diffusion rates under different potentials (**Figure 4d**). The BiOCl/MXene anode exhibited higher discharge potentials than BiOCl anode. This indicated the heterostructure can boost potassium ion diffusion and contribute to lower reaction barriers. As demonstrated in **Figure 4e and 4f**, the calculated diffusion coefficients D_{K+} ranging from 10^{-10} to 10^{-13} and D_{K+} in BiOCl/MXene anode was one order of magnitude bigger than

that in BiOCl anode, firmly elucidating the advantages of introducing MXene into BiOCl nanosheets. The heterointerface has provided a favorable environment for electron transfer and ion diffusion, promoting atomic dispersion of potassium ions and laying a solid foundation for stabilizing alloying/de-alloying processes.[53, 54]

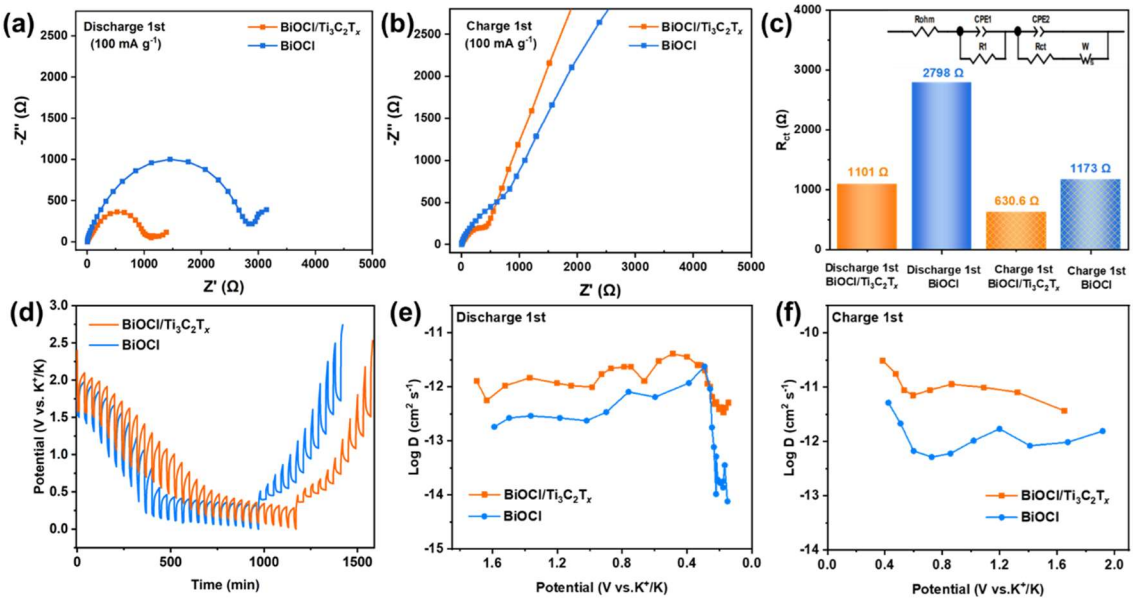

Figure 4 Electrochemical kinetics: a) Nyquist plots of BiOCl/$Ti_3C_2T_x$ MXene and BiOCl anodes at the full-discharge state; b) Nyquist plots of BiOCl/$Ti_3C_2T_x$ MXene and BiOCl anodes at the full-charge state; c) The calculated numerical values of charge transfer resistances of BiOCl/$Ti_3C_2T_x$ MXene and BiOCl anodes at full-discharge and full-charge states (the inset is the Randles equivalent electrical circuit); d) The GITT curves of BiOCl/$Ti_3C_2T_x$ MXene and BiOCl anodes; (e) The ion diffusion coefficients at different discharge states; and (f) The ion diffusion coefficients at different charge states.

The DFT-based first principles calculations were further performed to reveal the synergistic effects of BiOCl and $Ti_3C_2T_x$ MXene on potassium ion dispersion states. **Figure 5a** demonstrated two possible configurations for the BiOCl/$Ti_3C_2T_x$ MXene van der Waals heterostructure, where the (100) plane of BiOCl was assembled with (110) and (100) planes of MXenes, respectively. Based on the calculation results, the intercalation of potassium ions into MXenes with O terminals were much easier than that with F terminals and thus $Ti_3C_2O_2$ MXenes were chosen as the ideal model. In **Figure 5b**, $Ti_3C_2O_2$ (110)/BiOCl (100) displayed the lowest intercalation energy of -4.81 eV. This value was far lower than that of BiOCl, convincingly proving the introduction of MXenes can enhance the intercalation of potassium ions. The easier intercalation process agrees well with the electrochemical profile of the BiOCl/MXene anode and has created conditions for obtaining rich

atomically dispersed potassium ions. Moreover, compared with $Ti_3C_2O_2$ (100)/BiOCl (100), $Ti_3C_2O_2$ (110)/BiOCl (100) heterointerface was more energetically favorable for potassium ion intercalation. **Figure 5c** presented major diffusion pathways for potassium ions in BiOCl, $Ti_3C_2O_2$ (110)/BiOCl (100), and $Ti_3C_2O_2$ (100)/BiOCl (100) and their corresponding diffusion energy barriers were displayed in **Figure 5d**. The highly exposed (001) plane of BiOCl led more potassium ions to diffuse through van der Waals gaps and the diffusion barrier was 0.78 eV. After introducing MXene layers, the van der Waals Heterostructure enabled more facile potassium diffusion and obviously lower diffusion energy than single BiOCl nanosheets did. As anticipated, the diffusion barrier of $Ti_3C_2O_2$ (110)/BiOCl (100) (0.21 eV) was smaller than that of $Ti_3C_2O_2$ (100)/BiOCl (100) (0.61 eV). Therefore, we can safely come to the conclusion that the van der Waals heterointerface between BiOCl and MXenes may exceedingly boost potassium ion diffusion and contribute to atomic dispersion of potassium ions, which may enable more thorough and stable alloying/de-alloying reactions and help optimize potassium ion storage performance.

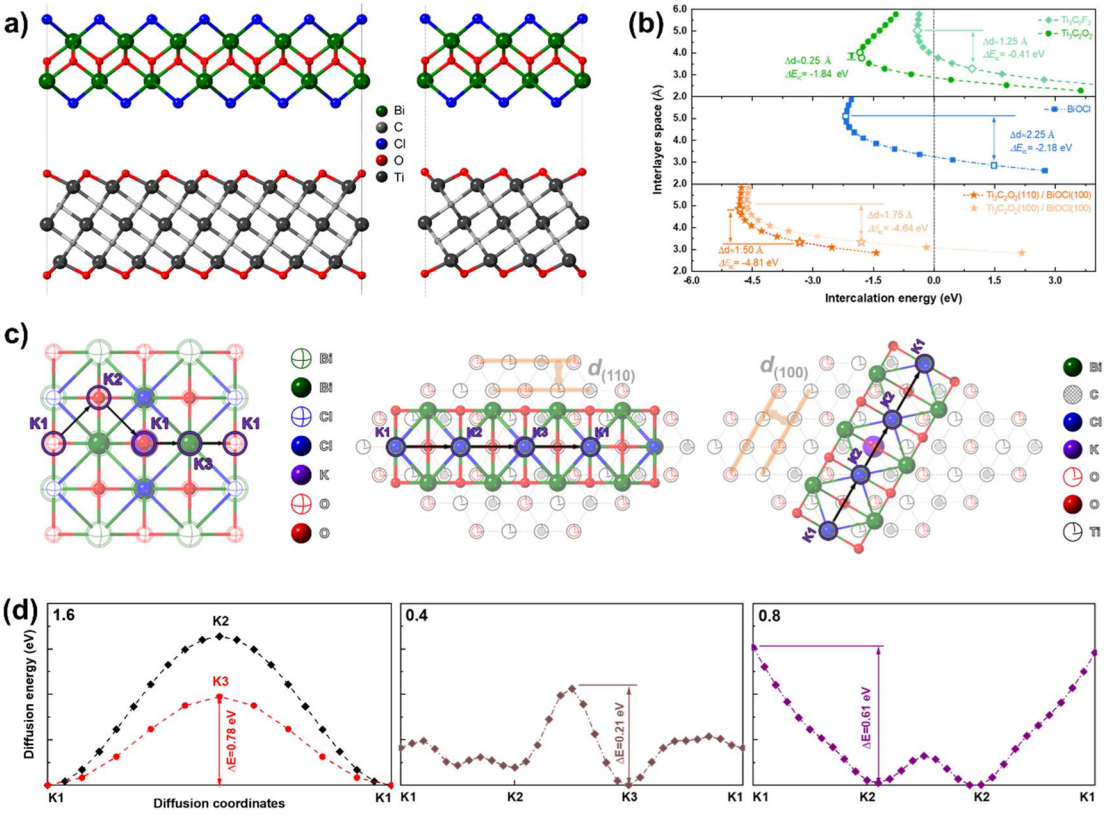

Figure 5 Theoretical calculations and potassium ion storage mechanism: a) Atomic configurations of $Ti_3C_2O_2$ (110)/BiOCl (100) (left), and $Ti_3C_2O_2$ (100)/BiOCl (100) (right); b) The intercalation energy of potassium ions in $Ti_3C_2F_2$, $Ti_3C_2O_2$, BiOCl, $Ti_3C_2O_2$ (110)/BiOCl (100), and $Ti_3C_2O_2$ (100)/BiOCl (100); c) Diffusion pathways of potassium ions in BiOCl, $Ti_3C_2O_2$ (110)/BiOCl (100), and $Ti_3C_2O_2$ (100)/BiOCl (100); d) Diffusion barriers of potassium ions in BiOCl, $Ti_3C_2O_2$ (110)/BiOCl (100), and $Ti_3C_2O_2$ (100)/BiOCl (100).

Operando X-ray diffraction has also been performed to better elucidate the potassium ion storage mechanism. The GCD curves of BiOCl/MXene anode at 50 mA g^{-1} and corresponding XRD patterns were shown in **Figure 6a**. The BiOCl/MXene anode fabricated here showed a typical electrochemical reaction mechanism like BiOCl. During the initial stage of discharge process, (101), (110), (102), (200) planes of BiOCl were observed at 25.8°, 32.5°, 33.4°, and 47°, except the distinct peaks assigned to BeO (at 38.8°, 41.4°, and 44°) and Be (at 46°). Intensities of these characterization peaks gradually decreased along with the conversion reaction of BiOCl, accompanied by the augmentation of (200) and (220) reflections of KCl. As the discharge process continued, new peak at 27.55° appeared and it belongs to bismuth metal. Subsequently, more peaks at 17.5°, 18.8°, and 27.2° can be noticed and they can be indexed to the (-211), (012), and (400) planes of KBi alloy. When attaining deeper discharge states, several peaks located at 20.4°, 28.8°, and 33.8° occurred, corresponding to (200), (220), and (311) planes of K_3Bi alloy. Note that the K_3Bi alloy formed here was cubic instead of hexagonal. This indicated atomic-level dispersion of potassium ions can be realized and more potassium ions can participate in the multi-step alloying process, leading to fully complete alloying reactions. During the following charge process, the reverse de-alloying reactions were observed as well. Based on the *operando* XRD analysis, an intensive investigation of the potassium ion storage behavior during the first cycle has been done in **Figure 6b** and **6c**. BiOCl/MXene anode exhibited higher discharge potential and lower charge potential compared with the BiOCl anode, indicating easier potassium diffusion processes, which was consistent with the calculation results. Notably, before the conversion stage, BiOCl/MXene anode went through potassium ion intercalation. Its intercalation reaction potential and intercalation capacity were obviously higher than the BiOCl anode. At the same time, for BiOCl/MXene anode, the conversion stage and alloying stage devoted higher capacities than those in the BiOCl anode, showing more thorough potassium ion storage reactions boosted by an atomic-level dispersion of potassium ions.

Post-mortem analysis has been further examined to explore the intrinsic origins of high cycling performance. **Figure S14a, 14b, and 14c** have shown the TEM images of BiOCl/MXene anodes which were first discharged to 0.01 V, first charged to 2.5 V, and discharged to 0.01 V for the second time. Their corresponding HRTEM images and XRD patterns were exhibited in **Figure 6d–6f** and **Figure 6k–6m**. At 0.01 V during the first discharge process, numerous particles were distributed

homogeneously between the MXene nanosheets by virtue of the heterointerface. The lattice spacing of these particles was 0.31 nm, which was in good agreement with the (220) plane of K_3Bi. The formation of K_3Bi were firmly confirmed and possessed cubic structure features, according to the diffraction peaks shown in XRD patterns. Meanwhile, the peak intensity ratio of K_3Bi to Bi in BiOCl/MXene anode was higher than BiOCl anode, meaning a more thorough alloying reaction. Furthermore, such a complete alloying process should be credited to the atomic dispersion of potassium ions, which can be supported by the microstructure observation results. As shown in **Figure 6j**, the HAADF-STEM image and corresponding EDS mappings of the first-discharged anode demonstrated that Bi and K elements were uniformly dispersed as alloy particles of about 10 nm confined between MXene nanosheets. Importantly, the potassium ions nearly can realize atomic-level dispersion with the help of the van der Waals heterostructure and this facilitated a complete alloying/de-alloying process, further promoting the reaction reversibility. In contrast, as shown in **Figure S15** Supporting Information, the discharge products of BiOCl anodes were mainly clumps of about 10 μm, exhibiting serious agglomeration and phase separation. Moreover, as demonstrated in **Figure 6g**, the full-discharged electrodes were mainly composed of unreacted large-size Bi metals and small-size K_3Bi alloys. This made it very hard for BiOCl anodes to experience stable alloying/de-alloying reactions. Continuously, at 2.5 V during the first charge process, for BiOCl/MXene anode, the charge products, bismuth particles, turned smaller and remained well restrained and distributed among the MXene skeletons, sustaining structure stability. Its corresponding XRD peak intensity ratio of Bi to KCl was higher than that of the BiOCl anode, embodying a good de-alloying process. No obvious peaks linked with BiOCl nanosheets were noticed and the conversion reaction from BiOCl to Bi was irreversible, which was consistent with the previously reported results.[38, 39, 55] In addition, for the BiOCl anode, the formed Bi metals showed smaller sizes and uneven distribution around the large-size bulk Bi metals (**Figure 6h**). Meanwhile, the XRD peak intensity ratio of Bi to KCl was expected to be higher than that of BiOCl anode discharging to 0.01 V during the first cycle, but actually, it decreased instead. This was linked with an incomplete de-alloying reaction and the BiOCl anode may have lower structure integrity towards a huge volume variation. To further validate the reaction reversibility, detailed morphology and structure characterizations towards the electrode at 0.01 V during the second discharge process have been executed. For BiOCl/MXene anode, the K_3Bi alloys were observed again and well

dispersed among MXene substrates, manifesting the high reversibility of the alloying/de-alloying reactions of bismuth. In contrast, as shown in **Figure 6i**, the discharge products of BiOCl anode were mainly broken K_3Bi particles and the bulk Bi particles were still unreacted. Besides, the XRD diffraction peak ratio of K_3Bi to Bi maintained a higher value than the BiOCl anode, confirming a reversible thorough alloying/de-alloying reaction. Moreover, a long-term post-mortem analysis has been carried out. **Figure S16** Supporting Information disclosed the SEM images of BiOCl/MXene and BiOCl anodes after 100 cycles at 100 mA g^{-1}. Severe particle pulverization and terrible distribution appeared in BiOCl anode and this was consistent with the fast capacity decay as described in **Figure 3c**. For comparison, BiOCl/MXene anode sustained the layered structure and effectively avoided breakage and agglomeration. It was worth mentioning that the electrochemical products maintained a good dispersion between MXene nanosheets and by virtue of the MXene supporting layers, the structural integrity was well-reserved and the volume change and self-aggregation were enormously alleviated. The impressive long cycling stability has precisely come from these above prominent strengths.

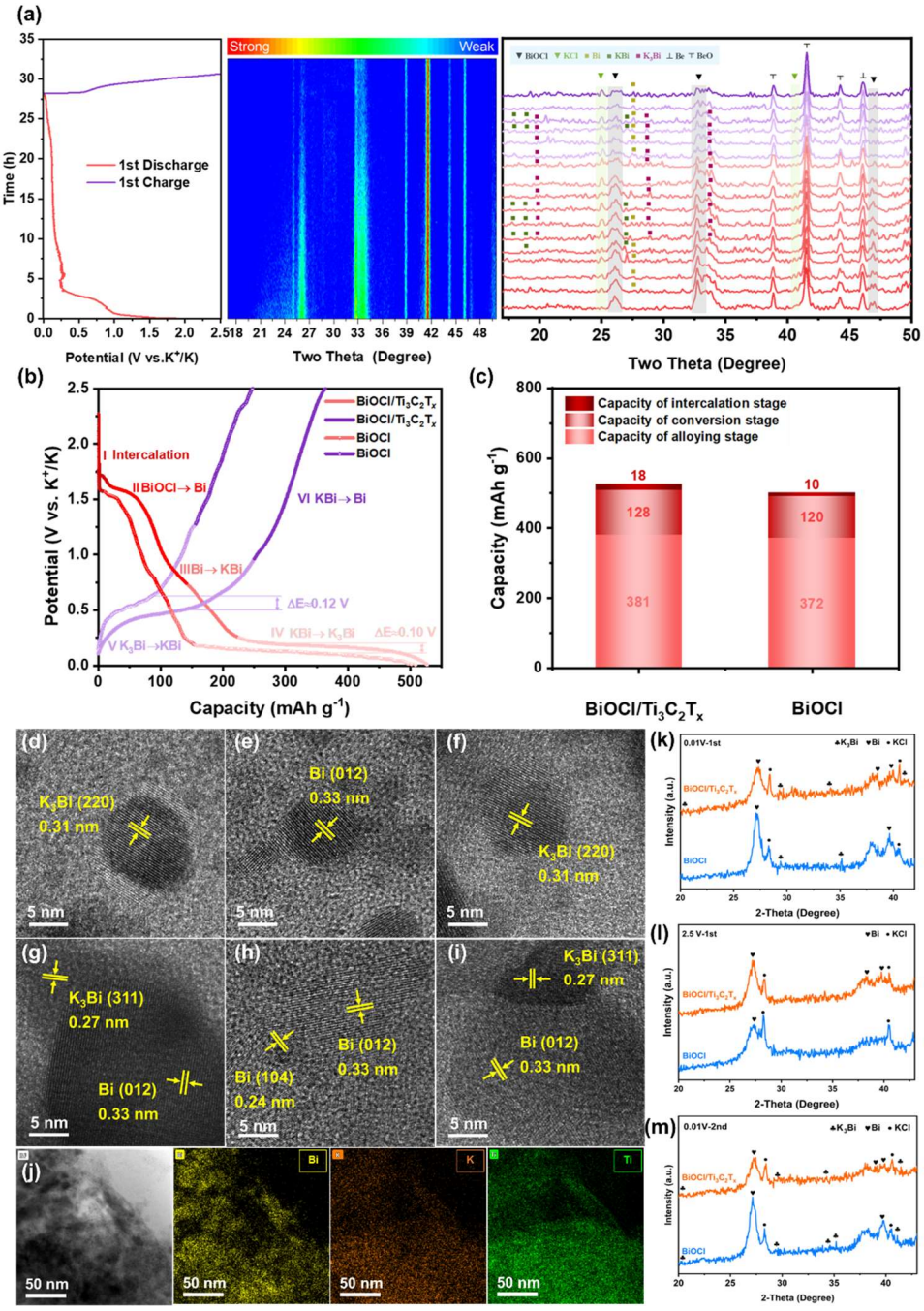

Figure 6 Potassium ion storage mechanism and post-mortem analysis: a) Operando X-ray diffraction patterns and corresponding GCD curves of BiOCl/MXene anodes; b) Proposed reaction mechanisms corresponding to GCD curves of BiOCl/MXene and BiOCl anodes based on the *operando* XRD results; c) Capacities of intercalation stage, conversion stage and alloying stage for BiOCl/MXene and BiOCl anodes; HRTEM images of BiOCl/MXene anodes d) at 0.01 V in the first discharge process, e) at 2.5 V in the first charge process, and f) at 0.01 V in the second discharge process; HRTEM images of BiOCl anodes g) at 0.01 V in the first discharge process, h) at 2.5 V in the first charge process, and i) at 0.01 V in the second discharge process; j) HAADF-STEM image and corresponding EDS mappings of BiOCl/MXene anode at 0.01 V in the first discharge process; XRD patterns of BiOCl/MXene and BiOCl anodes k) at 0.01 V in the first discharge process, l) at 2.5 V in the first charge process, and m) at 0.01 V in the first discharge process.

Hence, based on the above discussion, the principal reasons for the splendid cycling performance of BiOCl/MXene anode have been schematically illustrated in **Figure 7**:

(1) During the first cycle: the van der Waals heterointerface between MXene and BiOCl has offered facile diffusion paths for potassium ion intercalation, greatly enhancing potassium ion storage kinetics and enabling atomic dispersion of potassium ions. These rich atomic dispersed potassium ions can ensure highly reversible alloying/de-alloying reactions and help stimulate a long cycle life. In stark contrast, for bulk BiOCl anode, it was hard for potassium ions to diffuse evenly into the inner lattice of BiOCl, failing to form uniform alloy phases.

(2) During the subsequent cycling process: the MXene framework can support the alloy particles and help accommodate volume change during the cycling process, remarkably facilitating the structural integrity. On the contrary, without supporting MXene layers, bulk BiOCl anode suffered from bismuth loss and severe structure damage, experiencing incomplete and unstable alloying/de-alloying processes.

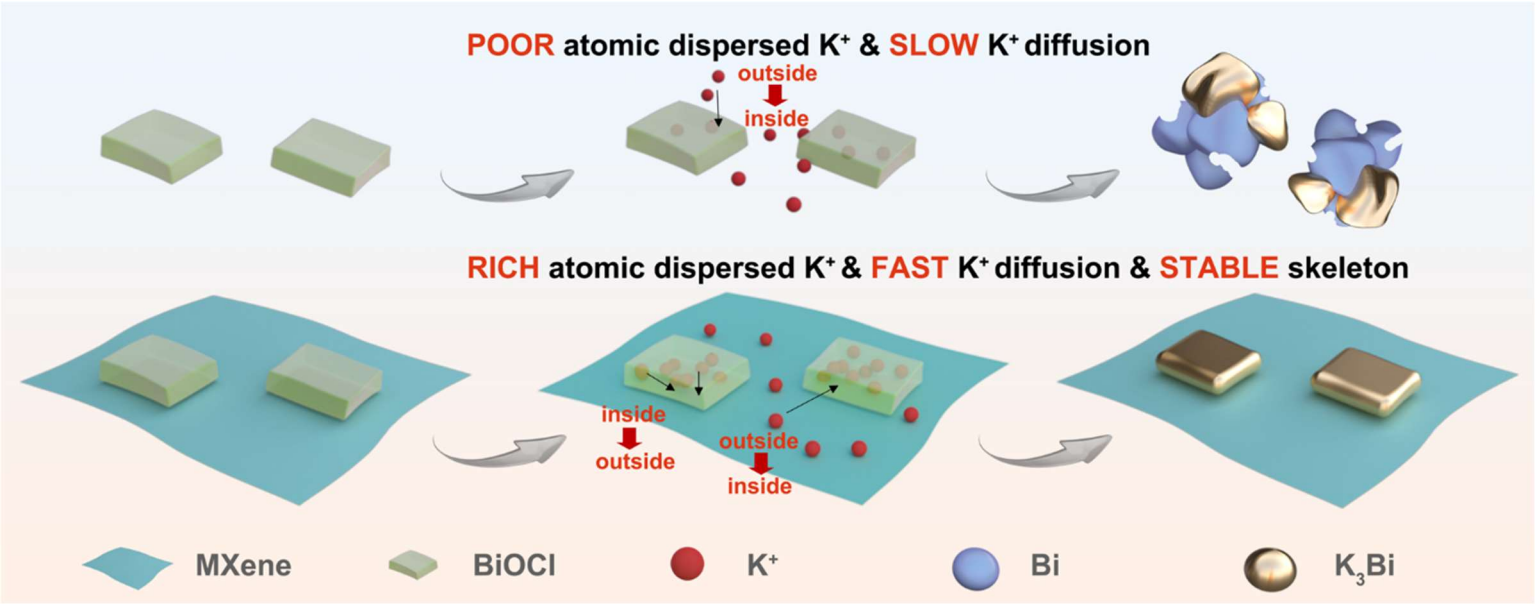

Figure 7 Schematic illustration of BiOCl/MXene and BiOCl anodes.

3. Conclusion

For the proof-of-concept demonstration, we have successfully established two model systems, BiOCl/$Ti_3C_2T_x$ MXene van der Waals heterostructure, and BiOCl, to disclose the relationship between potassium ion dispersion states and the potassium ion storage reaction reversibility. The

accelerated potassium ion diffusion kinetics in BiOCl/ $Ti_3C_2T_x$ MXene anode was found to result in richly dispersed potassium ions and thus to contribute to an enormously optimized intercalation process and to stabilize the alloying/de-alloying reactions. Correspondingly, the BiOCl/$Ti_3C_2T_x$ MXene anode exhibited an ultralong cycling performance of 225 mAh g^{-1} after 1335 cycles at such a small current density of 100 mA g^{-1}, running over ten months. Noteworthily, the excellent cycling stability obtained at a low current density has become evidently distinguished from the previous studies, propelling the commercial use of conversion/alloying-type anode materials. These findings are expected to develop a universal strategy for boosting cycling life by extending the law between ion dispersion states and reaction reversibility to other kinds of conversion/alloying-type anodes. These will also shed light on further optimization of high-performance anodes for alkali-metal-ion batteries.

Acknowledgements

The authors appreciate the financial funding from the National Key R&D Program of China (2021YFA1501502), National Natural Science Foundation of China (22075263, 52002366), Fundamental Research Funds for the Central Universities (WK2060000039), Natural Science Foundation of Jiangsu Province (No. BK20200386, No. BK20200406) and the China Scholarship Council (No.202206090249). The authors appreciate the supercomputing system in the Supercomputing Center of the University of Science and Technology of China, USTC Center for micro-and nanoscale research and fabrication, Beamlines MCD-A and MCD-B (Soochow Beamline for Energy Material) at National Synchrotron Radiation Laboratory (NSRL) in Hefei, China.

References

[1]Zhou, M.; Bai, P.; Ji, X.; Yang, J.; Wang, C.; Xu, Y., Electrolytes and Interphases in Potassium Ion Batteries. *Adv Mater* **2021,** *33* (7), e2003741.

[2]Fan, L.; Hu, Y.; Rao, A. M.; Zhou, J.; Hou, Z.; Wang, C.; Lu, B., Prospects of Electrode Materials and Electrolytes for Practical Potassium-Based Batteries. *Small Methods* **2021,** *5* (12), e2101131.

[3]Min, X.; Xiao, J.; Fang, M.; Wang, W.; Zhao, Y.; Liu, Y.; Abdelkader, A. M.; Xi, K.; Kumar, R. V.; Huang, Z., Potassium-ion batteries: outlook on present and future technologies. *Energy Environ Sci* **2021,** *14* (4), 2186-2243.

[4]Zhang, W.; Lu, J.; Guo, Z., Challenges and future perspectives on sodium and potassium ion batteries for grid-scale energy storage. *Mater Today* **2021,** *50*, 400-417.

[5]Hao, G.; Zhang, C.; Chen, Z.; Xu, Y., Nanoconfinement Synthesis of Ultrasmall Bismuth Oxyhalide Nanocrystals with Size-Induced Fully Reversible Potassium-Ion Storage and Ultrahigh Volumetric Capacity. *Adv Funct Mater* **2022,** *32* (27).

[6]Ma, L.; Li, X.; Li, Z.; Zhang, Y.; Ji, Z.; Wang, H.; Mai, W.; Li, J.; Pan, L., Bismuth oxychloride anchoring on graphene nanosheets as anode with a high relative energy density for potassium ion battery. *J Colloid Interface Sci* **2021,** *599*, 857-862.

[7]Xu, J.; Dou, S.; Cui, X.; Liu, W.; Zhang, Z.; Deng, Y.; Hu, W.; Chen, Y., Potassium-based electrochemical energy storage devices: Development status and future prospect. *Energy Storage Mater* **2021,** *34*, 85-106.

[8]Tian, X.; Zhang, P.; Liao, Y.; Soomro, R. A.; Xu, B., Achieving Stable and Ultrafast Potassium Storage of Antimony Anode via Dual Confinement of MXene@Carbon Framework. *Small Methods* **2023**, e2201525.

[9]Zhang, F.; Liu, X.; Wang, B.; Wang, G.; Wang, H., Bi@C Nanospheres with the Unique Petaloid Core-Shell Structure Anchored on Porous Graphene Nanosheets as an Anode for Stable Sodium- and Potassium-Ion Batteries. *ACS Appl Mater Interfaces* **2021,** *13* (50), 59867-59881.

[10]Yang, Q.; Li, H.; Feng, C.; Ma, Q.; Zhang, L.; Wang, R.; Liu, J.; Zhang, S.; Zhou, T.; Guo, Z.; Zhang, C., Encapsulation of BiOCl nanoparticles in N-doped carbon nanotubes as a highly efficient anode for potassium ion batteries. *Nanoscale* **2022,** *14* (15), 5814-5823.

[11]He, Y.; Gu, M.; Xiao, H.; Luo, L.; Shao, Y.; Gao, F.; Du, Y.; Mao, S. X.; Wang, C., Atomistic Conversion Reaction Mechanism of WO3 in Secondary Ion Batteries of Li, Na, and Ca. *Angew Chem Int Ed Engl* **2016,** *55* (21), 6244-7.

[12]Fang, L.; Wang, C.; Huangfu, L.; Bahlawane, N.; Tian, H.; Lu, Y.; Pan, H.; Yan, M.; Jiang, Y., Enabling Full Conversion Reaction with High Reversibility to Approach Theoretical Capacity for Sodium Storage. *Adv Functl Mater* **2019,** *29* (46).

[13]Du, X.; Huang, J.; Guo, X.; Lin, X.; Huang, J.-Q.; Tan, H.; Zhu, Y.; Zhang, B., Preserved Layered Structure Enables Stable Cyclic Performance of MoS2 upon Potassium Insertion. *Chem Mater* **2019,** *31* (21), 8801-8809.

[14]Sheng, J.; Wang, T.; Tan, J.; Lv, W.; Qiu, L.; Zhang, Q.; Zhou, G.; Cheng, H. M., Intercalation-Induced Conversion Reactions Give High-Capacity Potassium Storage. *ACS Nano* **2020,** *14* (10), 14026-14035.

[15]Du, X.; Gao, Y.; Zhang, B., Building Elastic Solid Electrolyte Interphases for Stabilizing Microsized Antimony Anodes in Potassium Ion Batteries. *Adv Funct Mater* **2021,** *31* (26).

[16]Luo, B.; Wu, P.; Zhang, J.; Cao, L.; Wang, C.; Lu, B.; Zhang, B.; Ou, X., Van der Waals heterostructure engineering by 2D space-confinement for advanced potassium-ion storage. *Nano Res* **2021,** *14* (11), 3854-3863.

[17]Biroju, R. K.; Das, D.; Sharma, R.; Pal, S.; Mawlong, L. P. L.; Bhorkar, K.; Giri, P. K.; Singh, A. K.; Narayanan, T. N., Hydrogen Evolution Reaction Activity of Graphene–MoS2 van der Waals Heterostructures. *ACS Energy Lett* **2017,** *2* (6), 1355-1361.

[18]Zhu, J.; Fan, J.; Cheng, T.; Cao, M.; Sun, Z.; Zhou, R.; Huang, L.; Wang, D.; Li, Y.; Wu, Y., Bilayer nanosheets of unusual stoichiometric bismuth oxychloride for potassium ion storage and CO2 reduction. *Nano Energy* **2020,** *75*.

[19]Ye, L.; Wang, L.; Xie, H.; Su, Y.; Jin, X.; Zhang, C., Two-Dimensional Layered BiOX (X=Cl, Br) Compounds as Anode Materials for Lithium-Ion Batteries. *Energy Technol* **2015,** *3* (11), 1115-1120.

[20]Zhang, P.; Soomro, R. A.; Guan, Z.; Sun, N.; Xu, B., 3D carbon-coated MXene architectures with high and ultrafast lithium/sodium-ion storage. *Energy Storage Mater* **2020,** *29*, 163-171.

[21]Zhang, P.; Li, J.; Yang, D.; Soomro, R. A.; Xu, B., Flexible Carbon Dots-Intercalated MXene Film Electrode with Outstanding Volumetric Performance for Supercapacitors. *Adv Funct Mater* **2022,** *33* (1).

[22]Qi, Q.; Zhang, H.; Zhang, P.; Bao, Z.; Zheng, W.; Tian, W.; Zhang, W.; Zhou, M.; Sun, Z., Self-assembled sandwich hollow porous carbon sphere @ MXene composites as superior LiS battery cathode hosts. *2D Mater* **2020,** *7* (2).

[23]Wang, B.; Wang, M.; Liu, F.; Zhang, Q.; Yao, S.; Liu, X.; Huang, F., Ti(3) C(2) : An Ideal Co-catalyst? *Angew Chem Int Ed Engl* **2020,** *59* (5), 1914-1918.

[24]Sarycheva, A.; Gogotsi, Y., Raman Spectroscopy Analysis of the Structure and Surface Chemistry of Ti3C2Tx MXene. *Chem Mater* **2020,** *32* (8), 3480-3488.

[25]Boota, M.; Anasori, B.; Voigt, C.; Zhao, M. Q.; Barsoum, M. W.; Gogotsi, Y., Pseudocapacitive Electrodes Produced by Oxidant-Free Polymerization of Pyrrole between the Layers of 2D Titanium Carbide (MXene). *Adv Mater* **2016,** *28* (7), 1517-22.

[26]Shuck, C. E.; Sarycheva, A.; Anayee, M.; Levitt, A.; Zhu, Y.; Uzun, S.; Balitskiy, V.; Zahorodna, V.; Gogotsi, O.; Gogotsi, Y., Scalable Synthesis of Ti3C2Tx MXene. *AdvEng Mater* **2020,** *22* (3).

[27]Wu, K.; Li, Z.; Tang, J.; Lv, X.; Wang, H.; Luo, R.; Liu, P.; Qian, L.; Zhang, S.; Yuan, S., Controllable defects implantation in MoS2 grown by chemical vapor deposition for photoluminescence enhancement. *Nano Res* **2018,** *11* (8), 4123-4132.

[28]Pang, R.; Tian, P.; Jiang, H.; Zhu, M.; Su, X.; Wang, Y.; Yang, X.;

Zhu, Y.; Song, L.; Li, C., Tracking structural evolution: operando regenerative CeO(x)/Bi interface structure for high-performance CO(2) electroreduction. *Natl Sci Rev* **2021,** *8* (7), nwaa187.

[29]Cao, J.; Cen, W.; Jing, Y.; Du, Z.; Chu, W.; Li, J., P-doped BiOCl for visible light photodegradation of tetracycline: An insight from experiment and calculation. *ChemEng J* **2022,** *435*.

[30]Zhao, Z.; Cao, Y.; Dong, F.; Wu, F.; Li, B.; Zhang, Q.; Zhou, Y., The activation of oxygen through oxygen vacancies in BiOCl/PPy to inhibit toxic intermediates and enhance the activity of photocatalytic nitric oxide removal. *Nanoscale* **2019,** *11* (13), 6360-6367.

[31]Zhao, L.; Wang, L.; Zheng, Y.; Zhao, S.; Wei, W.; Zhang, D.; Fu, X.; Jiang, K.; Shen, G.; Han, W., Highly-stable polymer-crosslinked 2D MXene-based flexible biocompatible electronic skins for in vivo biomonitoring. *Nano Energy* **2021,** *84*.

[32]Wu, S.; Su, Y.; Zhu, Y.; Zhang, Y.; Zhu, M., In-situ growing Bi/BiOCl microspheres on Ti3C2 nanosheets for upgrading visible-light-driven photocatalytic activity. *Appl Surf Sci* **2020,** *520*.

[33]Yan, J.; Ren, C. E.; Maleski, K.; Hatter, C. B.; Anasori, B.; Urbankowski, P.; Sarycheva, A.; Gogotsi, Y., Flexible MXene/Graphene Films for Ultrafast Supercapacitors with Outstanding Volumetric Capacitance. *Adv Funct Mater* **2017,** *27* (30).

[34]Huang, J.; Lin, X.; Tan, H.; Zhang, B., Bismuth Microparticles as Advanced Anodes for Potassium-Ion Battery. *Adv Energy Mater* **2018,** *8* (19).

[35]Lei, K.; Wang, C.; Liu, L.; Luo, Y.; Mu, C.; Li, F.; Chen, J., A Porous Network of Bismuth Used as the Anode Material for High-Energy-Density Potassium-Ion Batteries. *Angew Chem Int Ed Engl* **2018,** *57* (17), 4687-4691.

[36]Wang, J.; Fan, L.; Liu, Z.; Chen, S.; Zhang, Q.; Wang, L.; Yang, H.; Yu, X.; Lu, B., In Situ Alloying Strategy for Exceptional Potassium Ion Batteries. *ACS Nano* **2019,** *13* (3), 3703-3713.

[37]Zhang, R.; Bao, J.; Wang, Y.; Sun, C. F., Concentrated electrolytes stabilize bismuth-potassium batteries. *Chem Sci* **2018,** *9* (29), 6193-6198.

[38]Yao, J.; Zhang, C.; Yang, G.; Sha, M.; Dong, Y.; Fu, Q.; Wu, Y.; Zhao, H.; Wu, M.; Lei, Y., Bismuth Nanoparticles Confined in Carbonaceous Nanospheres as Anodes for High-Performance Potassium-Ion Batteries. *ACS Appl Mater Interfaces* **2021,** *13* (27), 31766-31774.

[39]Li, W.; Xu, Y.; Dong, Y.; Wu, Y.; Zhang, C.; Zhou, M.; Fu, Q.; Wu, M.; Lei, Y., Bismuth oxychloride nanoflake assemblies as a new anode for potassium ion batteries. *Chem Commun* **2019,** *55* (46), 6507-6510.

[40]Cheng, X.; Li, D.; Wu, Y.; Xu, R.; Yu, Y., Bismuth nanospheres embedded in three-dimensional (3D) porous graphene frameworks as high performance anodes for sodium- and potassium-ion batteries. *J Mater Chem A* **2019,** *7* (9), 4913-4921.

[41]Fang, S.-J.; Du, P.; Zhang, J.-F.; Wang, C.-H.; Xiao, Z.-M.; Zhang, B.; Cao, L.; Fan, X.-M.; Ou, X., Quasi-two-dimensional bismuth oxychalcogenide nanoflakes as novel anode for potassium-ion batteries. *Rare Metals* **2022,** *41* (8),

2567-2574.
[42]He, X.-D.; Liao, J.-Y.; Wang, S.; Wang, J.-R.; Liu, Z.-H.; Ding, X.; Hu, Q.; Wen, Z.-Y.; Chen, C.-H., From nanomelting to nanobeads: nanostructured SbxBi1−x alloys anchored in three-dimensional carbon frameworks as a high-performance anode for potassium-ion batteries. *J Mater Chem A* **2019,** *7* (47), 27041-27047.
[43]Hu, J.; Xie, Y.; Zheng, J.; Lai, Y.; Zhang, Z., Unveiling nanoplates-assembled Bi2MoO6 microsphere as a novel anode material for high performance potassium-ion batteries. *Nano Res* **2020,** *13* (10), 2650-2657.
[44]Liu, Y.; Li, M.; Zheng, Y.; Lin, H.; Wang, Z.; Xin, W.; Wang, C.; Du, F., Boosting potassium-storage performance via the functional design of a heterostructured Bi2S3@RGO composite. *Nanoscale* **2020,** *12* (48), 24394-24402.
[45]Liu, Z.; Zhao, S.; Li, G.; Chen, C.; Xie, X.; Wu, Z.; Zhang, N., Stabilizing BiOCl/Ti3C2Tx hybrids for potassium-ion batteries via solid electrolyte interphase reconstruction. *Inorg Chem Front* **2022,** *9* (13), 3165-3175.
[46]Qin, Y.; Zhang, Y.; Wang, J.; Zhang, J.; Zhai, Y.; Wang, H.; Li, D., Heterogeneous Structured Bi2S3/MoS2@NC Nanoclusters: Exploring the Superior Rate Performance in Sodium/Potassium Ion Batteries. *ACS Appl Mater Interfaces* **2020,** *12* (38), 42902-42910.
[47]Su, S.; Liu, Q.; Wang, J.; Fan, L.; Ma, R.; Chen, S.; Han, X.; Lu, B., Control of SEI Formation for Stable Potassium-Ion Battery Anodes by Bi-MOF-Derived Nanocomposites. *ACS Appl Mater Interfaces* **2019,** *11* (25), 22474-22480.
[48]Wu, Q.; Chen, B.; Xie, H.; Bai, X.; Liang, M.; Wu, Z.; Jin, X.; He, C.; Zhao, N., Bismuth-antimony alloy nanoparticles encapsulated in 3D carbon framework: Synergistic effect for enhancing interfacial potassium storage. *Chem Eng J* **2022,** *430*.
[49]Xiang, X.; Liu, D.; Zhu, X.; Fang, K.; Zhou, K.; Tang, H.; Xie, Z.; Li, J.; Zheng, H.; Qu, D., Evaporation-induced formation of hollow bismuth@N-doped carbon nanorods for enhanced electrochemical potassium storage. *Appl Surf Sci* **2020,** *514*.
[50]Xie, F.; Zhang, L.; Chen, B.; Chao, D.; Gu, Q.; Johannessen, B.; Jaroniec, M.; Qiao, S.-Z., Revealing the Origin of Improved Reversible Capacity of Dual-Shell Bismuth Boxes Anode for Potassium-Ion Batteries. *Matter* **2019,** *1* (6), 1681-1693.
[51]Yang, H.; Xu, R.; Yao, Y.; Ye, S.; Zhou, X.; Yu, Y., Multicore–Shell Bi@N-doped Carbon Nanospheres for High Power Density and Long Cycle Life Sodium- and Potassium-Ion Anodes. *Adv Funct Mater* **2019,** *29* (13).
[52]Zhao, X.; Zhang, C.; Yang, G.; Wu, Y.; Fu, Q.; Zhao, H.; Lei, Y., Bismuth selenide nanosheets confined in thin carbon layers as anode materials for advanced potassium-ion batteries. *Inorg Chem Front* **2021,** *8* (18), 4267-4275.
[53]Zhou, G.; Wang, B.; Cao, R., Acid Catalysis in Confined Channels of Metal-Organic Frameworks: Boosting Orthoformate Hydrolysis in Basic Solutions. *J Am Chem Soc* **2020,** *142* (35), 14848-14853.
[54]Wordsworth, J.; Benedetti, T. M.; Somerville, S. V.; Schuhmann, W.; Tilley,

R. D.; Gooding, J. J., The Influence of Nanoconfinement on Electrocatalysis. *Angew Chem Int Ed Engl* **2022,** *61* (28), e202200755.

[55]Wang, J.; Wang, B.; Lu, B., Nature of Novel 2D van der Waals Heterostructures for Superior Potassium Ion Batteries. *Adv Energy Mater* **2020,** *10* (24).